



This is a repository copy of *Low dielectric loss, and enhanced magneto-dielectric properties of Cu_{0.5}Cd_{0.5}-CoFe₂O₄ ferrites via Co²⁺ substitution.*

White Rose Research Online URL for this paper:

<https://eprints.whiterose.ac.uk/197492/>

Version: Accepted Version

Article:

Rehman, A.U., Sharif, S., Hegazy, H.H. et al. (7 more authors) (2023) Low dielectric loss, and enhanced magneto-dielectric properties of Cu_{0.5}Cd_{0.5}-CoFe₂O₄ ferrites via Co²⁺ substitution. *Materials Today Communications*, 34. 105371. ISSN 2352-4928

<https://doi.org/10.1016/j.mtcomm.2023.105371>

Article available under the terms of the CC-BY-NC-ND licence
(<https://creativecommons.org/licenses/by-nc-nd/4.0/>).

Reuse

This article is distributed under the terms of the Creative Commons Attribution-NonCommercial-NoDerivs (CC BY-NC-ND) licence. This licence only allows you to download this work and share it with others as long as you credit the authors, but you can't change the article in any way or use it commercially. More information and the full terms of the licence here: <https://creativecommons.org/licenses/>

Takedown

If you consider content in White Rose Research Online to be in breach of UK law, please notify us by emailing eprints@whiterose.ac.uk including the URL of the record and the reason for the withdrawal request.



eprints@whiterose.ac.uk
<https://eprints.whiterose.ac.uk/>

Low dielectric loss, and enhanced magneto-dielectric properties of $Cu_{0.5}Cd_{0.5-x}Co_xFe_2O_4$ ferrites via Co^{2+} substitution

Atta Ur Rehman^a, Sehrish Sharif^a, Maria Akhtar^a, Nasir Amin^a, Nicola Morley^b, Muhammad Imran Arshad^{a*}, Hafiz T Ali^c, M. Yusuf^d, Mongi Amami^{e,f}, Lamia Ben Farhat^{e,f}

^aDepartment of Physics, Government College University, Faisalabad, Pakistan.

^bDepartment of Materials Science and Engineering, The University of Sheffield, UK, S1 3JD.

^cDepartment of Mechanical Engineering, College of Engineering, Taif University, P.O. Box 1109, Taif 21944, Saudi Arabia

^dDepartment of Clinical Pharmacy, College of Pharmacy, Taif University, P.O. Box 1109, Taif 21944, Saudi Arabia.

^eDepartment of Chemistry College of Sciences, King Khalid University, P.O. Box 9004, Abha, Saudi Arabia

^fLaboratoire des Matériaux et de l'environnement pour le développement durable LR18ES10. 9 Avenue Dr. Zoheir SAFI, 1006, Tunis, Tunisia

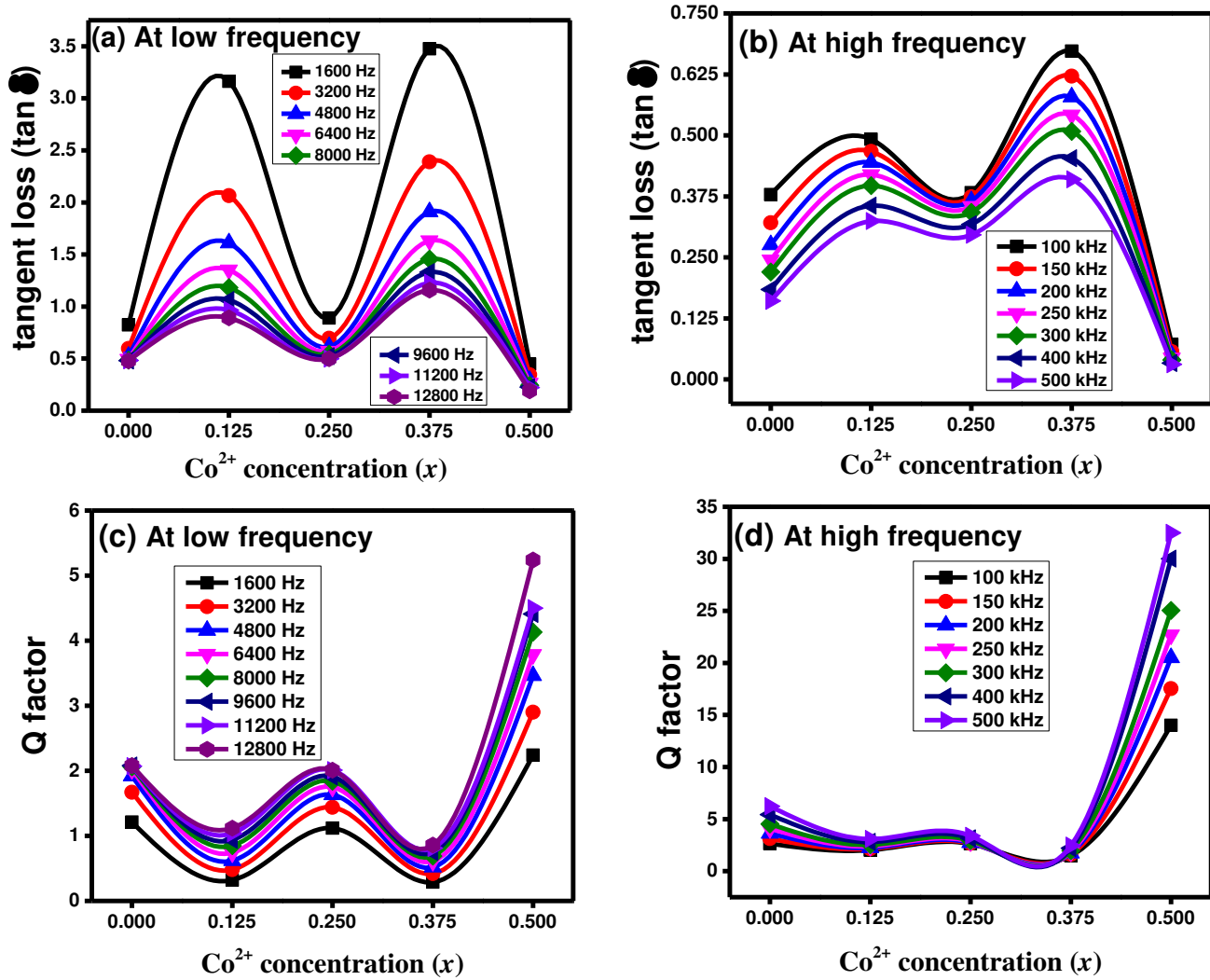
*Corresponding Author: miarshadgcuf@gmail.com

Abstract

Spinel ferrites (SFs) with composition $Cu_{0.5}Cd_{0.5-x}Co_xFe_2O_4$ ($x = 0.0, 0.125, 0.25, 0.375, 0.5$) were prepared via **the** effective and low-cost sol-gel auto combustion process. X-ray diffraction confirmed the single-phase spinel matrix. Furthermore, with increasing Co^{2+} ions doping the lattice constant (a) was reduced and crystal size increased. The variation in two major absorption and vibration bands at tetrahedral and octahedral sites also confirmed the substitution of dopant ions in lattice sites. Moreover, the bandgap energy was measured using UV-visible analysis and was increased with the doping of Co^{2+} and **was 2.44 eV for $x = 0.375$** . At 313 K, the **highest** electrical resistivity and activation energy **were $7.17 \times 10^8 \Omega \text{ cm}$ and 0.44 eV** , respectively for the sample **$x = 0.375$** . The **maximum** dielectric constant and tangent loss was observed, while the Q factor was **minimum** for **sample $x = 0.375$** (as clear from the graphical abstract). The coercivity was **536.82 Oe** and saturation magnetization **had** a value of **128.49 emu/g** with microwave frequency **28.40 GHz** for sample **$x = 0.375$** . The following results suggested that the sample with $x = 0.375$ is useful for high-frequency resonant circuits and multilayer chip inductors applications.

Keywords: sol-gel auto combustion; single-phase; resistivity; magnetization; microwave.

Graphical Abstract



Highlights

- Low-cost, and effective sol-gel auto combustion synthesis of $\text{Cu}_{0.5}\text{Cd}_{0.5-x}\text{Co}_x\text{Fe}_2\text{O}_4$.
- The crystal size was observed at 46.61 nm and the optical bandgap was found 2.44 eV for sample $x = 0.375$.
- The highest electrical resistivity and the activation energy were $7.17 \times 10^8 \Omega \text{ cm}$ and 0.44 eV for sample $x = 0.375$.
- The maximum dielectric tangent loss and minimum Q factor were observed for $x = 0.375$.
- The saturation magnetization was maximum for sample $x = 0.375$.

1 Introduction

Spinel ferrites (SFs) have gained enormous consideration due to their unique characteristics including high coercivity, low eddy current loss, low magnetization, and high resistivity. The SFs have the general formula MFe_2O_4 where M is divalent ions including Mg^{2+} , Cu^{2+} , Co^{2+} , Zn^{2+} , and Cd^{2+} , etc. The SFs structure is a cubic closely packed oxygen atoms arrangement in which the oxygen layer contains 32 octahedral (B -) and 64 tetrahedral (A -) sites [1]. The inversion parameter (δ) is used to describe the cation distribution, which is dependent on the synthesis process and composition [2]. With $\delta = 0$, Cd^{2+} cations occupy A -sites, and Fe^{3+} cations occupy B -sites, bulk cadmium ferrite ($CdFe_2O_4$) is a normal spinel [3]. Cu^{2+} and Co^{2+} cations occupy B - sites, and only a limited quantity of Cu^{2+} and Co^{2+} ions migrate from the B -sites to the A - sites in copper ferrite ($CuFe_2O_4$) and cobalt ferrite ($CoFe_2O_4$), respectively. These are known as a partially inverted ($\delta \rightarrow 1$) spinel matrix [4, 5]. Numerous investigations have been done on the results of Cu [6-10], Cd [11-14], Co [15-21], Cu-Cd [22], Cu-Co [23], Co-Cd [24], and Cu-Cd-Co [25] ferrites. The properties of SFs are affected by dopant ions. The best of our research indicates that there are few reports on $Cu_{0.5}Cd_{0.5-x}Co_xFe_2O_4$ ($x = 0.0, 0.125, 0.25, 0.375, 0.5$) ferrite powder.

The unique characteristics of low-cost copper metal and the advancement of fabrication methods for $CuFe_2O_4$ ferrite with distinct physical properties have opened up numerous possibilities for its use in different applications including photocatalysts [6], lithium-ion batteries [7, 8], energy storage material [9], and photoanodes for solar water oxidation [10]. Normal spinel matrix and nonmagnetic character can be seen in bulk $CdFe_2O_4$. Cd ferrite is used for different applications including photocatalytic degradation [11], ethanol sensing [12, 13], and gas sensing [14], whereas in the nano range, an inverted spinel matrix with improved magnetic properties has been observed [26]. The initial permeability and density of the ferrites increase as a result of the incorporation of Cd^{2+} ions, and the magnetic loss factor decreases [27]. Because of its high anisotropy constant, high coercivity, and low magnetization, $CoFe_2O_4$ ferrite is used in a variety of applications in medicine (for example DNA isolation [15], magnetic resonance imaging (MRI) contrast agents [16], and magnetically activated medication delivery [17]) to electronics (for example microwave frequency [18], and optoelectronics [18], Magnetostrictive and gas sensors [28]). $CoFe_2O_4$ is a promising candidate for biosensors [19], heating agents of magnetic hyperthermia [20], targeting drug delivery carriers [21] due to the remarkable changes made to

specific parameters including DC resistivity, particle size, saturation magnetization, and initial permeability by transforming the bulk material into the nanostructure. Gabal *et al.*, [22] reported $Cu_{0.5}Cd_{0.5}Fe_2O_4$ (Cu-Cd) ferrite synthesized by metal oxalate thermal decomposition method and observed a lattice constant of 8.473 Å along with an X-ray density of 5.758 g/cm³. Farooq *et al.*, [23] prepared $Cu_{0.6}Co_{0.4}Fe_2O_4$ (Cu-Co) ferrite using the co-precipitation route and stated a lattice constant of 8.401 Å. The crystallite size of 35.48 nm and X-ray density of 5.318 g/cm³ was observed. Moreover, the electrical resistivity of $6.48 \times 10^8 \Omega \text{ cm}$ and bandgap energy of 2.05 eV were reported. The resistivity of the Cu-Co ferrite is of the order of $10^8 \Omega \text{ cm}$ used for telecommunication devices. Asghar *et al.*, [24] reported that $Co_{0.3}Cd_{0.7}Fe_2O_4$ (Co-Cd) ferrite has a crystallite size of 9.284 nm. The as-synthesized Co-Cd ferrites revealed paramagnetic behaviour and promising candidate for high-density memory devices and transformers applications. Hussain *et al.*, [25] reported co-precipitation preparation of $Cu_{0.5}Cd_{0.25}Co_{0.25}Fe_2O_4$ (Cu-Cd-Co) ferrite and their structural, optoelectrical, magnetic, and dielectric properties. They reported experimental lattice constant was 8.4693 Å and the crystallite size was 31.24 nm. Also, the electrical resistivity is $9.902 \times 10^7 \Omega \text{ cm}$ and has a bandgap energy is 3.48 eV. The coercivity has a value of 675 Oe, and magnetization is 23.29 emu/g. Moreover, such material is useful for transformers, and deflection yolks.

If the material is synthesized on a nanoscale with attention by managing the preparation method, the predicted change in numerous parameters for any given application can be made available to a greater extent. Co-precipitation route [25, 29-31], reverse micelle [32], a sol-gel auto-combustion (SGAC) technique [33-39], ultrasound irradiation method [40], microemulsion method [32], and hydrothermal route [41] are the most common synthesis methods. The SGAC synthesis method has shown incredible potential in the preparation of SFs. The following are some of the benefits of the SGAC route: (i) process initiates at low temperatures; (ii) high product crystallinity and purity; (iii) low processing time; (iv) good chemical homogeneity [42].

In this article, we have reported the influence of Co^{2+} doping on spectral, optical, electrical, dielectric, and magnetic properties of $Cu_{0.5}Cd_{0.5-x}Co_xFe_2O_4$ [Co-CCF] ($x = 0.0, 0.125, 0.25, 0.375, 0.5$) SFs prepared by SGAC process. Because of low losses, high coercivity, low magnetization, high resistivity, good chemical stability, and high Curie temperature, Cu-Cd, Cu-Co, and Cu-Cd-Co ferrites are one of the promising soft ferrites used in electronic devices like

telecommunication devices, deflection yolks, high-density memory devices, and transformers applications.

2 Experimental parts

2.1 Samples preparation method

The Co^{2+} doped Cu-Cd SFs powder was prepared through **the** sol-gel auto-combustion method with composition $\text{Cu}_{0.5}\text{Cd}_{0.5-x}\text{Co}_x\text{Fe}_2\text{O}_4$ ($x = 0.0, 0.125, 0.25, 0.375, 0.5$). The following metal nitrates including $\text{Cu}(\text{NO}_3)_2 \cdot 3\text{H}_2\text{O}$, $\text{Cd}(\text{NO}_3)_2 \cdot 4\text{H}_2\text{O}$, $\text{Co}(\text{NO}_3)_2 \cdot 6\text{H}_2\text{O}$, and $\text{Fe}(\text{NO}_3)_3 \cdot 9\text{H}_2\text{O}$ were utilized for sample preparation. To synthesize Co-CCF SFs, nitrates and citric acid were taken 1:1 and separately dissolved in deionized water. The $\text{pH} \sim 7$ was maintained with the addition of ammonia dropwise. The solution was continuously stirred and formed **a** gel at 573 K. Finally, after a few minutes, the gel was transformed into fluffy powder by auto-combustion. The combusted fluffy ferrite powder was sintering at 1023 K for 8 h and grounded to convert it into fine powder. This fine powder is used to perform different characterizations. The pictorial illustration of the synthesis procedure is given in [Fig. 1](#).

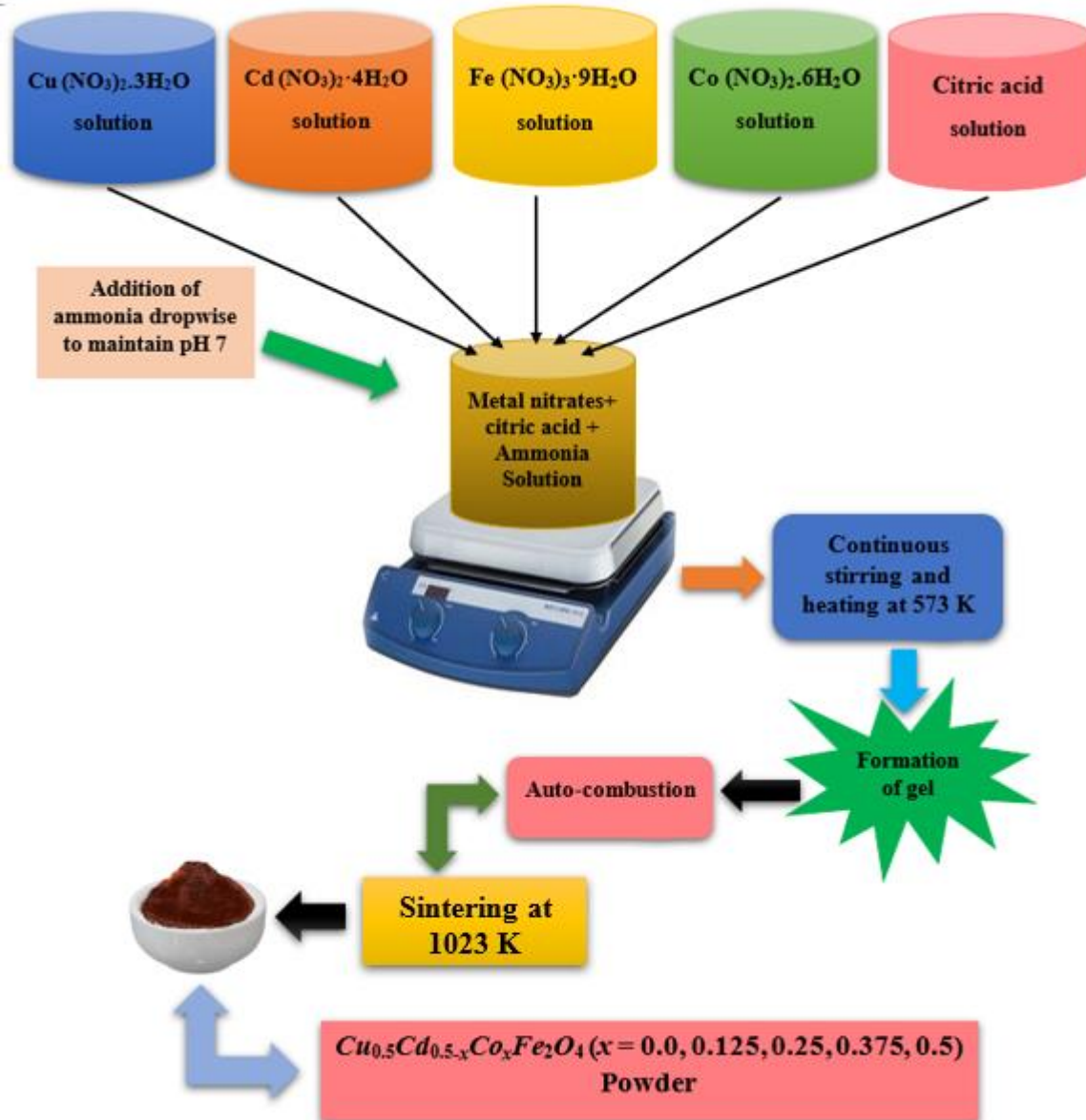


Fig. 1 Pictorial representation for the synthesis of Co-CCF samples

2.2 Characterization performed

X-ray diffraction (XRD) spectra of Co-CCF samples were measured through Bruker Advance Diffractometer. Absorption band spectra were obtained using FTIR spectroscopy. A UV-visible spectrophotometer was employed to evaluate the optical bandgap. LCR Meter (IM3536 model) was employed to record the dielectric parameters at room temperature (RT). Keithley Electrometer Model 2400 was used to measure the resistivity using the two probes *I-V* measurement technique. To record the magnetic behaviour of the ferrites, a vibrating sample magnetometer (VSM), Model VSM-175 was utilized in the range of ± 5000 Oe.

3 Results and discussion

3.1 Structural analysis

XRD spectra of Co-CCF powder samples are depicted in Fig. 2. The single-phase spinel cubic matrix was confirmed with the labeled peaks (220), (311), (222), (400), (422), and (511) [25, 43]. The experimental lattice constant (a) was determined and the unit cell volume (V_{cell}) using relation (1) and (2) [43], respectively.

$$a = \frac{\lambda}{2\sin\theta} \sqrt{h^2 + k^2 + l^2} \quad (1)$$

$$V_{\text{cell}} = a^3 \quad (2)$$

The determined values of “ a ” are given in Table 1 and value of “ a ” was 8.412 Å for pure Cu-Cd ferrites ($x = 0.0$), which then reduced from 8.487 Å to 8.371 Å with the insertion of Co^{2+} ions ($x = 0.125 - 0.5$) in the lattice. The interplanar spacing (d) and values of “ V_{cell} ” also decreased with the doping of Co^{2+} ions (Table 1). The substitution of smaller ionic radii Co^{2+} (0.74 Å) with larger ionic radii Cd^{2+} (0.78 Å) is responsible for the decreasing lattice constant [23]. Furthermore, the decline is caused by the shifting of the most conspicuous peak (311) and the decreasing behaviour of interplanar spacing [23]. The crystallite size (D) of the Co-CCF materials was estimated via the Scherrer formula [43, 44];

$$D = \frac{K\lambda}{\beta\cos\theta} \quad (3)$$

The “ D ” of the as-synthesized ferrites is seen in Table 1 and the values of “ D ” decreased with increasing the doping of Co^{2+} ions up to $x = 0.125$ and then crystallite size increased with increasing Co^{2+} concentration from $x = 0.25$ to $x = 0.5$. The pictorial representation of Co^{2+} doping versus crystallite size and lattice constant is given in Fig. 3. The intensity of diffraction peaks reduced with an increase in Co^{2+} doping, which indicates that the increase in the Co^{2+} ion content ($x = 0.125$) decreases the crystallite size, and further increasing the Co^{2+} concentration ($x = 0.25 - 0.5$) increased the crystallite size. The result revealed that a low concentration of Co^{2+} ions controls and retards the growth of the crystallite size, while high doping level of Co^{2+} favors the growth of the crystallite size at the nucleation centers, which resulted in higher crystallite size [45]. The hopping lengths (H_A , H_B) and polaron radius (γ) were determined by employing the relations (4), (5), and (6) [25, 43], respectively.

$$H_A = \frac{a\sqrt{3}}{4} \quad (4)$$

$$H_B = \frac{a\sqrt{2}}{4} \quad (5)$$

$$\gamma = \frac{1}{2} \sqrt[3]{\frac{\pi a^3}{576}} \quad (6)$$

Table 1 revealed that with the addition of Co^{2+} ions, tetrahedral (H_A) and octahedral (H_B) hopping lengths were reduced. It may be owing to the decrease in the lattice constant of as-synthesized Co-CCF samples. The hopping lengths and polaron radius behaved similarly and declined as the Co^{2+} doping increased.

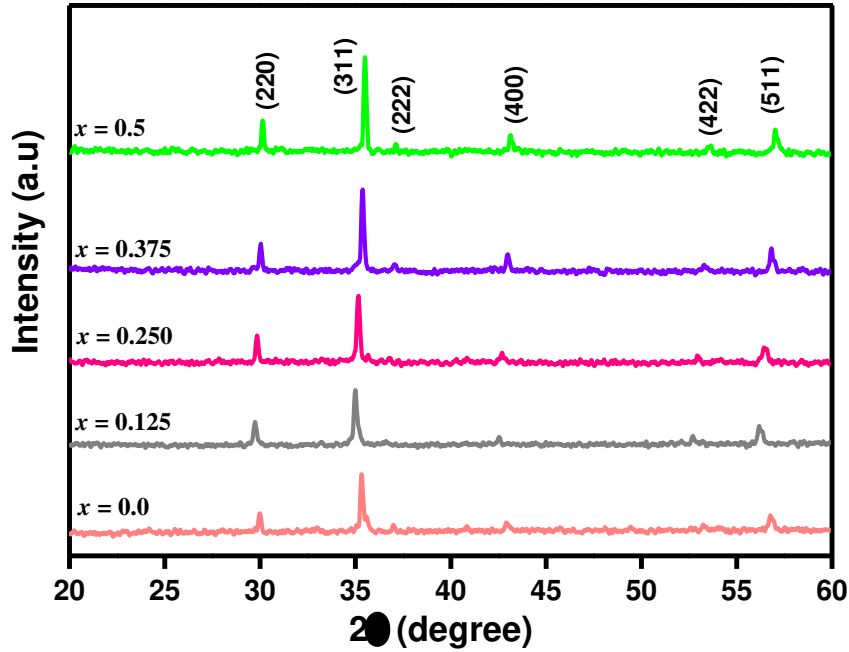


Fig. 2 XRD spectra for Co-CCF samples

Table 1 Structural parameters of Co-CCF samples

x	D (nm)	d (Å)	a (Å)	$\delta \times 10^{-4}$ (nm ⁻²)	V_{cell} (Å) ³	H_A (Å)	H_B (Å)	γ_p (Å)
0.0	42.36	2.536	8.412	5.57	595.37	3.642	2.973	0.753
0.125	35.76	2.558	8.487	7.81	611.31	3.674	3.000	0.760
0.25	42.28	2.549	8.454	5.59	604.27	3.660	2.988	0.757
0.375	46.61	2.533	8.403	4.60	593.41	3.638	2.970	0.752
0.5	50.88	2.524	8.371	3.86	586.64	3.624	2.959	0.749

The estimated cation distribution for Co-CCF samples is shown in Table 2. The CoFe_2O_4 (4% Co^{2+} ions reside at A - sites and 96% ions reside at B -sites) and CuFe_2O_4 (25% Cu^{2+} ions reside at A - sites and 75% Cu^{2+} ions reside at B -sites) ferrites have an inverse spinel structure

[46, 47]. Cd^{2+} ions prefer to reside on A-sites and ions of Fe^{3+} reside at both A- and B-sites [48]. The cationic radii at tetrahedral (r_A) and octahedral (r_B) sites were estimated via relations (7) and (8), respectively, and are given in Table 2.

$$r_A = (C_{\text{Cu}^{2+}}^A)(r_{\text{Cu}^{2+}}) + (C_{\text{Cd}^{2+}}^A)(r_{\text{Cd}^{2+}}) + (C_{\text{Co}^{2+}}^A)(r_{\text{Co}^{2+}}) + (C_{\text{Fe}^{3+}}^A)(r_{\text{Fe}^{3+}}) \quad (7)$$

$$r_B = \frac{1}{2} [(C_{\text{Cu}^{2+}}^B)(r_{\text{Cu}^{2+}}) + (C_{\text{Co}^{2+}}^B)(r_{\text{Co}^{2+}}) + (C_{\text{Fe}^{3+}}^B)(r_{\text{Fe}^{3+}})] \quad (8)$$

where C is the concentration of the composition ions (Cu, Cd, Co, and Fe). The ionic radii of Co^{2+} are 0.74 Å for B-site and 0.58 Å for A-site [49]. The cationic radii of Cd^{2+} are 0.78 Å, for Fe^{3+} ions are 0.645 Å for B-site and 0.49 Å for A-site [49]. The Cu^{2+} ion has ionic radii of 0.72 Å for the B-site and 0.57 Å for the A-site [49]. The theoretical lattice constant (a_{th}) was determined using relation (9) [50];

$$a_{th} = \frac{8}{3\sqrt{3}} [(r_A + R_o) + \sqrt{3}(r_B + R_o)] \quad (9)$$

It was clear from Table 2 that the value of “ a_{th} ” was reduced with the addition of dopant ions whereas both “ a ” and “ a_{th} ” versus Co^{2+} concentration (x) are depicted in Fig. 3. The theoretical lattice constant values are close in agreement with the experimental lattice constant. There is a mismatch between the host site radius and the ionic radius of the substitute ions due to an increase in the lattice constant because the replacement ions fill up a large space as the dopant concentration increases, and the lattice constant increases as well [51].

Table 2 Estimated cation distribution, tetrahedral and octahedral radii with theoretical lattice constant of Co-CCF samples

x	Lattice site		Ionic radii		Theoretical lattice constant
	A-site	B-site	r_A (Å)	r_B (Å)	a_{th} (Å)
0	($\text{Cu}_{0.125}\text{Cd}_{0.5}\text{Fe}_{0.375}$) _A	[$\text{Cu}_{0.375}\text{Fe}_{1.625}$] _B	0.645	0.661	8.307
0.125	($\text{Cu}_{0.125}\text{Cd}_{0.375}\text{Co}_{0.005}\text{Fe}_{0.495}$) _A	[$\text{Cu}_{0.375}\text{Co}_{0.12}\text{Fe}_{1.505}$] _B	0.609	0.666	8.265
0.25	($\text{Cu}_{0.125}\text{Cd}_{0.25}\text{Co}_{0.01}\text{Fe}_{0.615}$) _A	[$\text{Cu}_{0.375}\text{Co}_{0.24}\text{Fe}_{1.385}$] _B	0.573	0.672	8.226
0.375	($\text{Cu}_{0.125}\text{Cd}_{0.125}\text{Co}_{0.015}\text{Fe}_{0.735}$) _A	[$\text{Cu}_{0.375}\text{Co}_{0.36}\text{Fe}_{1.265}$] _B	0.537	0.678	8.187
0.5	($\text{Cu}_{0.125}\text{Co}_{0.02}\text{Fe}_{0.855}$) _A	[$\text{Cu}_{0.375}\text{Co}_{0.48}\text{Fe}_{1.145}$] _B	0.502	0.683	8.146

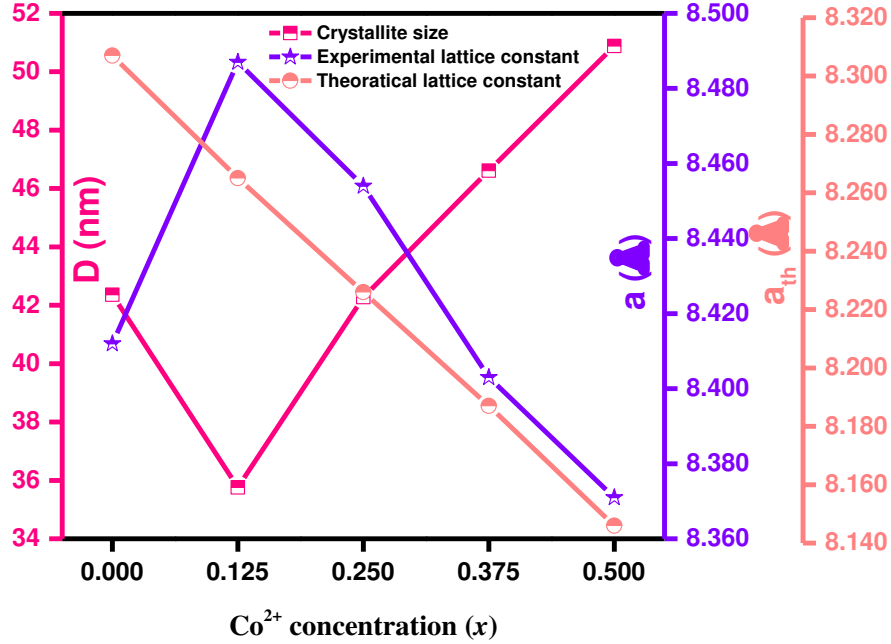


Fig. 3 Co²⁺ concentration (x) versus crystallite size, experimental and theoretical lattice constants

3.2 Absorption bands analysis

The Co-CCF sample's FTIR spectra are represented in Fig. 4 in the frequency range of 400–3500 cm⁻¹. The FTIR spectra indicate two main absorption bands ~400 cm⁻¹ and ~600 cm⁻¹ for the octahedral (B) site and tetrahedral (A) site [52], respectively. Fig. 4 shows variations in the shifting of bands and broadening of the absorption peaks with increasing Co²⁺ concentration (x). The main reason for the shift and broadening in absorption peaks are replacement of dopant ions in the replacement of Fe³⁺ ions with dopant ions at tetrahedral and octahedral sites of the spinel ferrites [53]. The A - and B - sites in a spinel matrix are allocated to the higher (ν_1) and lower (ν_2) frequency bands, having ranges (513 – 539 cm⁻¹) and (419 – 472 cm⁻¹), respectively (Table 3). The absorption bands are ~1600 cm⁻¹ due to H–O–H group and absorbing ~2350 cm⁻¹ is attributed to atmospheric CO₂ [54]. The force constant (K) was determined by employing the equation (10) [55];

$$K = 4\pi^2 \nu^2 c^2 m \quad (10)$$

' c ' is the speed of the light (3×10^{10} cm/s), ' ν ' is the absorption band for both sites, and ' m ' is the reduced mass (2.601×10^{-23} g) [54]. The force constant at tetrahedral (K_1) and octahedral (K_2) sites increased with the increasing Co²⁺ concentration (as seen in Table 3) due to the movement of O²⁻ ions towards Fe³⁺ ions at lattice sites as a result of charge imbalance caused by Fe³⁺ ion

migration from $A-$ to $B-$ sites. This movement causes a decrease in bond length and, as a result, an increase in the force constant [56].

Table 3 Absorption bands and force constants of as-prepared samples

x	ν_1 (cm^{-1})	ν_2 (cm^{-1})	$K_1 \times 10^5$ (dyne cm^{-1})	$K_2 \times 10^5$ (dyne cm^{-1})
0.0	513	419	2.43	1.62
0.125	527	461	2.56	1.96
0.25	531	462	2.61	1.97
0.375	533	463	2.63	1.99
0.5	539	472	2.68	2.05

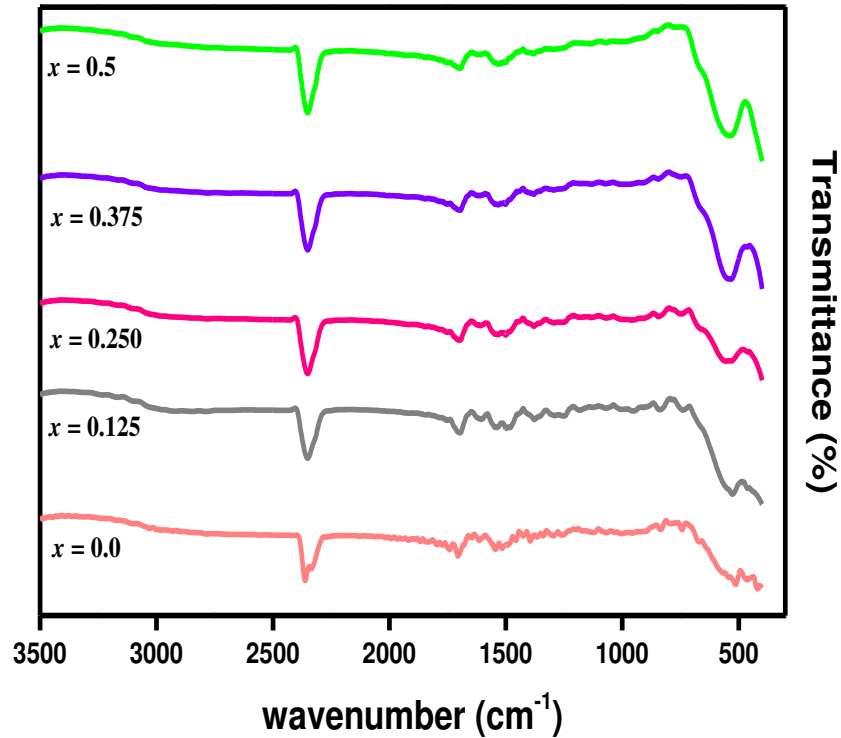


Fig. 4 FTIR spectra for Co-CCF samples

3.3 Vibrational modes analysis

Raman patterns were measured in the range of 200 to 800 cm^{-1} and depicted in Fig. 5(a-d) for samples $x = 0.0, 0.125, 0.25,$ and $0.375,$ respectively. According to group theory, the

vibrational modes of spinel/inverse spinel cubic structure owned by the ($F d -3 m$) space group, are below [57];

$$\Gamma = A_{1g}(R) + E_g(R) + T_{1g} + 3T_{2g}(R) + 2A_{2u} + 2E_u + 5T_{1u}(IR) + 2T_{2u} \quad (11)$$

where A_{1g} , E_g , and $3T_{2g}$ are fundamental active Raman modes. The observed values of all the Raman modes in the as-prepared Co-CCF samples are given in Table 4. The vibrational band “ $T_{1g}(1)$ ” and “ A_{1g} ” were found in the range of $292.73 - 299.08 \text{ cm}^{-1}$ and $664.31 - 688.45 \text{ cm}^{-1}$ respectively belonging to the tetrahedral site. The octahedral site vibrational bands “ E_g ”, $T_{1g}(2)$ and $T_{1g}(3)$ lie in the range of $328.77 - 386.91 \text{ cm}^{-1}$, $468.87 - 478.19 \text{ cm}^{-1}$, and $540.98 - 615.40 \text{ cm}^{-1}$, respectively.

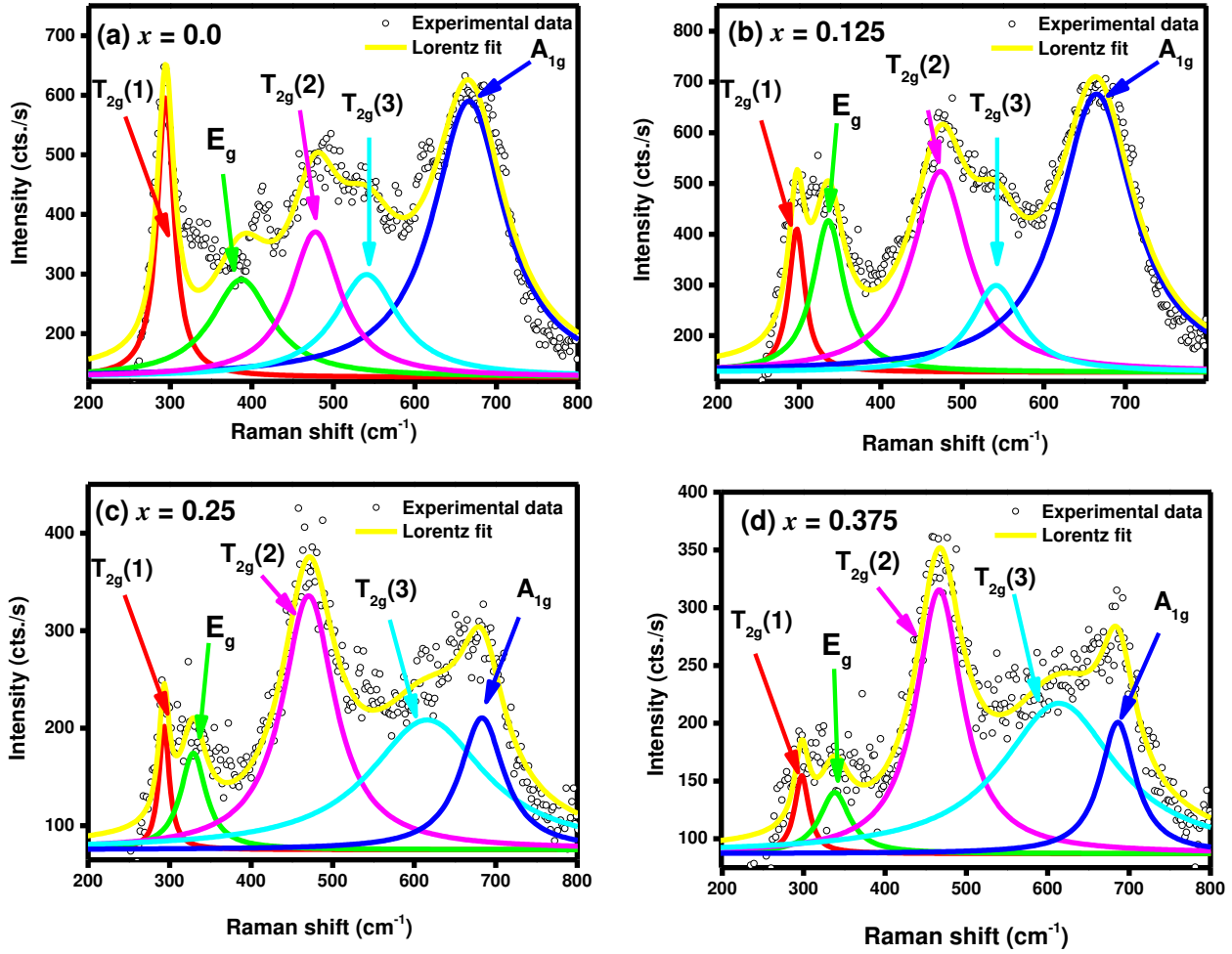


Fig. 5(a-d) Raman spectra for Co-CCF samples

Table 4 Raman modes for Co-CCF samples

x	Raman shift (cm ⁻¹)				
	$T_{2g}(1)$	E_g	$T_{2g}(2)$	$T_{2g}(3)$	A_{1g}
	Tetrahedral (A) site		Octahedral (B) site		Tetrahedral (A) site
0.0	292.73	386.91	478.19	540.98	666.68
0.125	297.56	336.40	473.90	541.05	664.31
0.25	293.61	328.77	469.47	615.40	681.11
0.375	299.08	337.52	468.87	611.57	688.45

3.4 Optical bandgap energy analysis

To calculate the optical bandgap energy of Co-CCF samples Tauc's plots were used and are depicted in Fig. 6(a-e). The optical bandgap energy (E_g) was estimated using Tauc's equation [50, 58];

$$(\alpha h\nu)^2 = B (E_g - h\nu) \quad (12)$$

where “ B ” is the proportionality constant, “ $h\nu$ ” is light energy, and “ α ” is the absorption coefficient. In spinel ferrites, the optical bandgap energy values depend on the lattice constant, with a decrease in the bandgap energy values being correlated with an increase in the lattice constant and vice versa [59, 60]. In the present case, the lattice constant decreased with the increasing the Co^{2+} ions concentration, which is related to an increase in optical bandgap energy. The optical bandgap values were observed at 1.77 eV, 1.80 eV, 2.29 eV, 2.44 eV, and 2.62 eV for Co^{2+} concentration enhanced from $x = 0.0$ to $x = 0.5$ in Co-CCF samples. Fig. 6(a-e) also revealed that the values of “ E_g ” were increased with the doping of Co^{2+} in the CCF lattice.

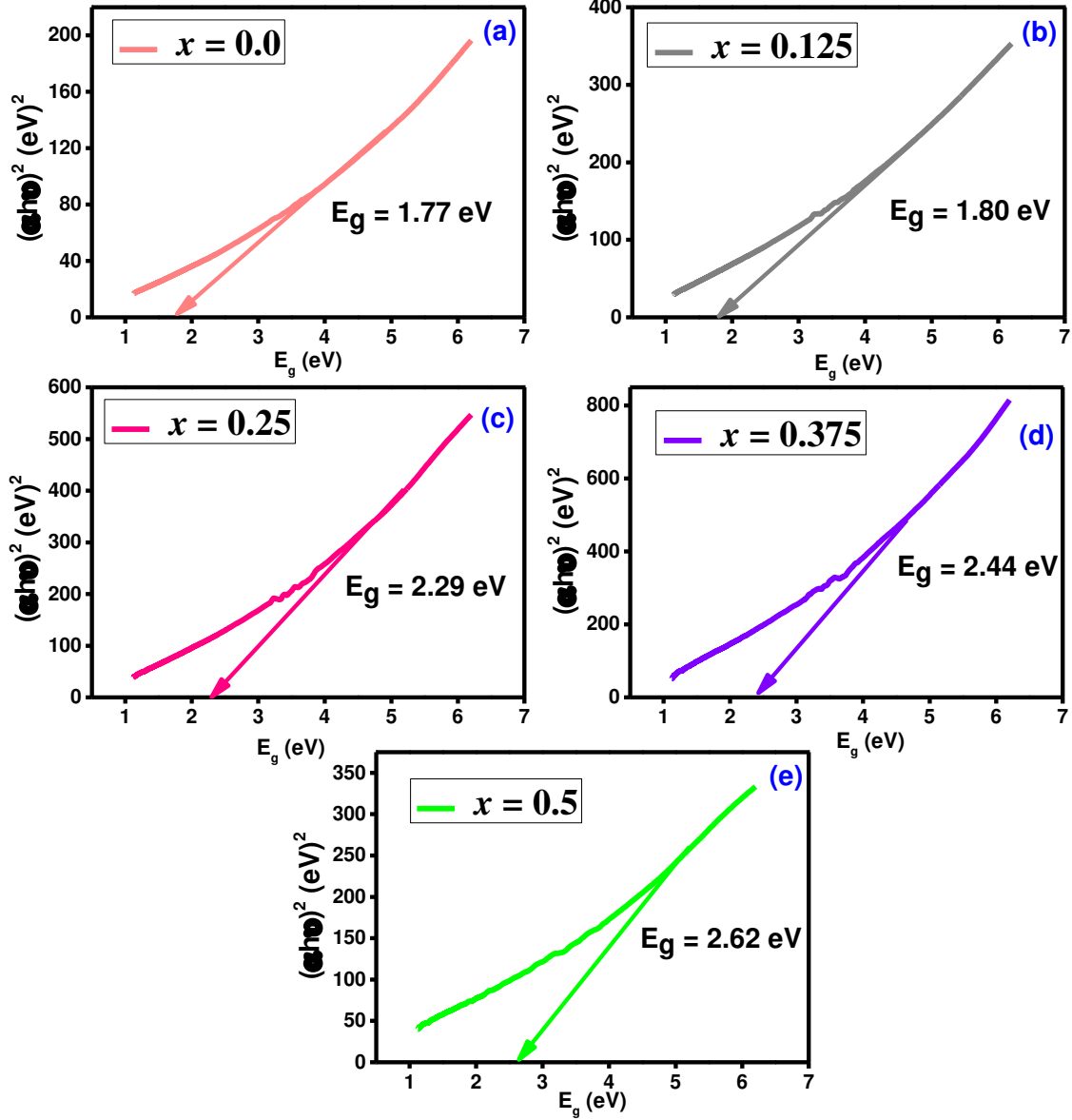


Fig. 6(a-e) Tauc's plots for Co-CCF samples

3.5 Current-voltage (I-V) analysis

The characteristics of certain materials by which they create hindrances in flow electrons are called electrical resistivity and are calculated using [61];

$$\rho = \frac{RA}{L} \quad (13)$$

where “R” was calculated as $R = 1/\text{slope}$ from current-voltage curves, “A” is the area and “L” referred to the thickness of prepared pellets. In solids, resistivity is highly sensitive to its defect formation and stoichiometric composition [61]. Fig. 7 depicted the Arrhenius plots. The

temperature at which the nature of material changes is called Curie temperature (T_C) and is given in Table 5. Fig. 7 shows in the ferro region (low-temperature region) the resistivity was maximum for $x = 0.0$ and in the para region (high-temperature region) the maximum resistivity was found for sample $x = 0.375$. The process known as Verwey's hopping is used to explain this resistivity behaviour. According to that process, spinel ferrites conduct due to electronic exchange between Fe^{2+} and Fe^{3+} ions located on the B - site. The distance between ions and activation energy has a huge impact on the hopping process. When compared to the distance between two metal ions on the A - and B - sites, the two metal ions at B -site are substantially closer to each other. As a result, hopping between two metal ions on the same site is significantly easier than hopping between two distinct sites. As a result, there is no hopping between the A - and B - sites since Fe^{3+} ions only exist at B - site and Fe^{2+} ions are accommodated on the B - site [61]. For the activation energy of samples, the slope of each resistivity curve (as illustrated in Fig. 7) was taken, and the relation (14) [50] was used to determine the activation energy.

$$E_a = 2.303 \times k_B \times 1000 \times slope \text{ (eV)} \quad (14)$$

The activation energy in SFs originates from the charge carrier's mobility and is affected by dopant ion replacement in the lattice. The activation energy and hopping process are inextricably related, and the resistivity follows the same pattern as the activation energy [62]. The activation energy and resistivity were reduced with the substitution of Co^{2+} ions (as seen in Table 5 and Fig. 8) at 313 K (room temperature). Fig. 9(a) and Fig. 9(b) represent the Co^{2+} concentration (x) versus resistivity at low temperature (383 K – 503 K) and resistivity at high temperature (523 K – 773 K). It was noted from Fig. 9(a) and Fig. 9(b) that at low and high temperatures the resistivity was maximum at Co^{2+} concentration $x = 0.375$.

Table 5 Electrical parameters of Co-CCF samples

Co ²⁺ content (x)	Resistivity $\times 10^8$ at 313 K (Ω cm)	Curie Temperature (K)	Activation energy (eV)
0.0	18.21	323	0.74
0.125	4.46	343	0.48
0.25	4.58	343	0.45
0.375	7.17	353	0.44
0.5	1.15	333	0.38

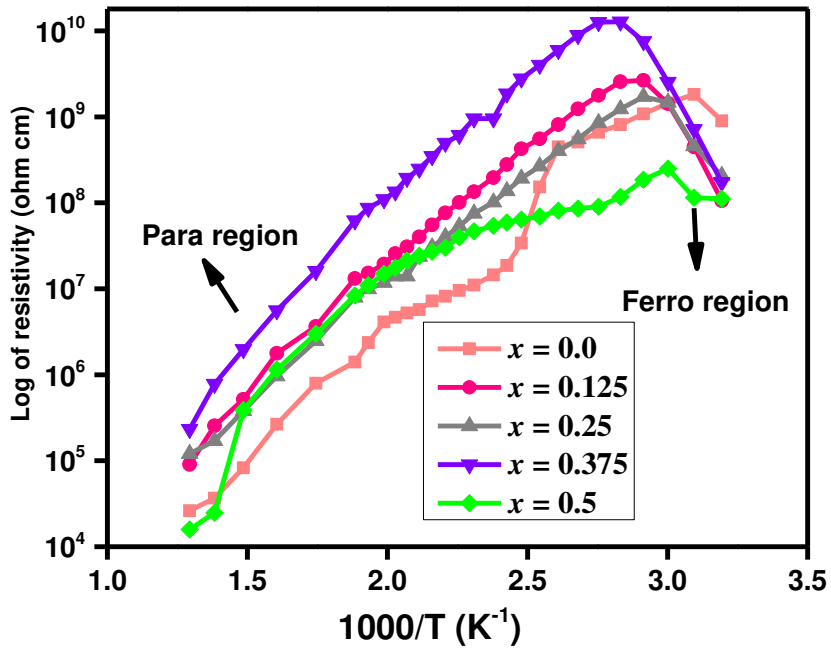


Fig. 7 Arrhenius plots of Co-CCF samples

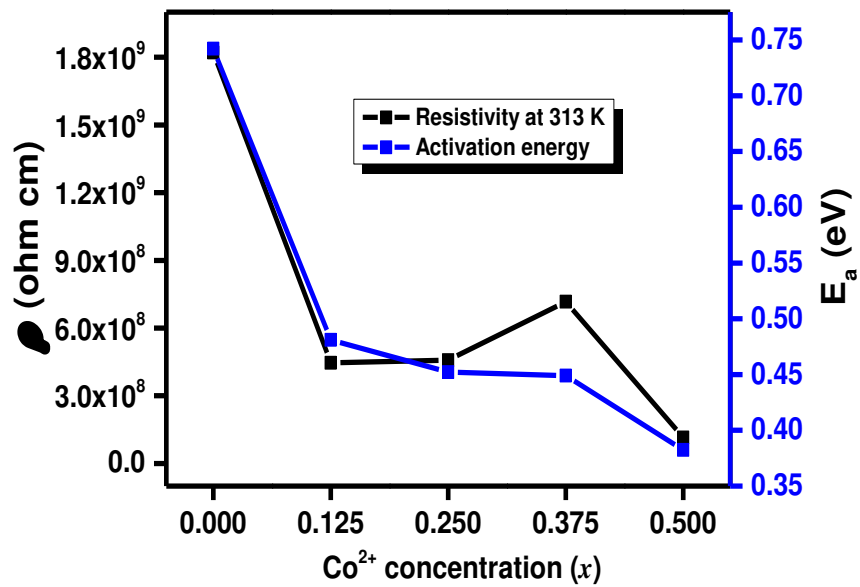


Fig. 8 Co^{2+} concentration (x) versus resistivity at 313 K and activation energy

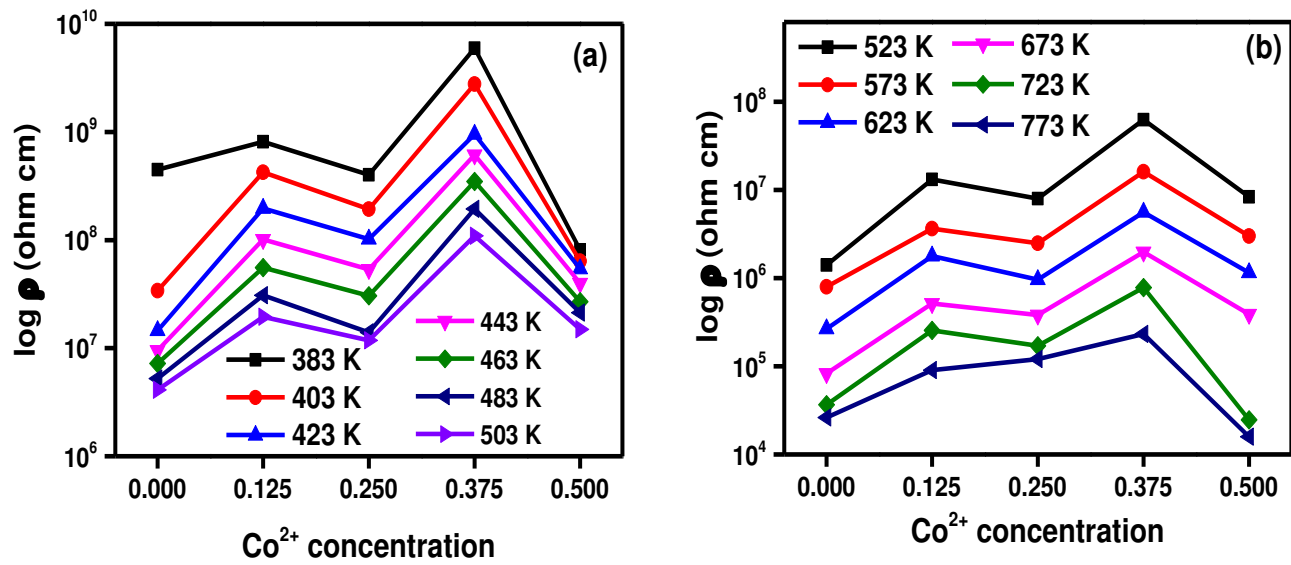


Fig. 9 Co^{2+} concentration (x) versus (a) log of resistivity at low temperature (383 K – 503 K) and (b) log of resistivity at high temperature (523 K – 773 K)

3.6 Dielectric analysis

The dependency of the Co-CCF sample's dielectric constant (ϵ') on frequency is shown in Fig. 10(a). The value of ϵ' was reduced by enhancing the frequency. The high value of ϵ' was related to the contributions from space charge, interface, and ionic polarization at lower frequencies. At high frequencies, the dielectric constant showed frequency-independent behaviour because of the instability of dipoles to obey the rapid alteration of the applied field. The reduction in the ϵ' with rising frequency is due to the theory of Koop and Maxwell–Wagner [63]. Fig. 10(b) indicates the dielectric tangent loss ($\tan \delta$) and frequency relation for Co-CCF samples. The values of “ $\tan \delta$ ” revealed a similar trend to the values of ϵ' . With increasing frequency, the “ $\tan \delta$ ” was reduced and at low frequency, the “ $\tan \delta$ ” has a maximum value as compared to high frequency. The dielectric loss is induced by impurities, defects, and grain boundaries, in the spinel matrix, and is linked with a lag in polarization with respect to the applied field [63].

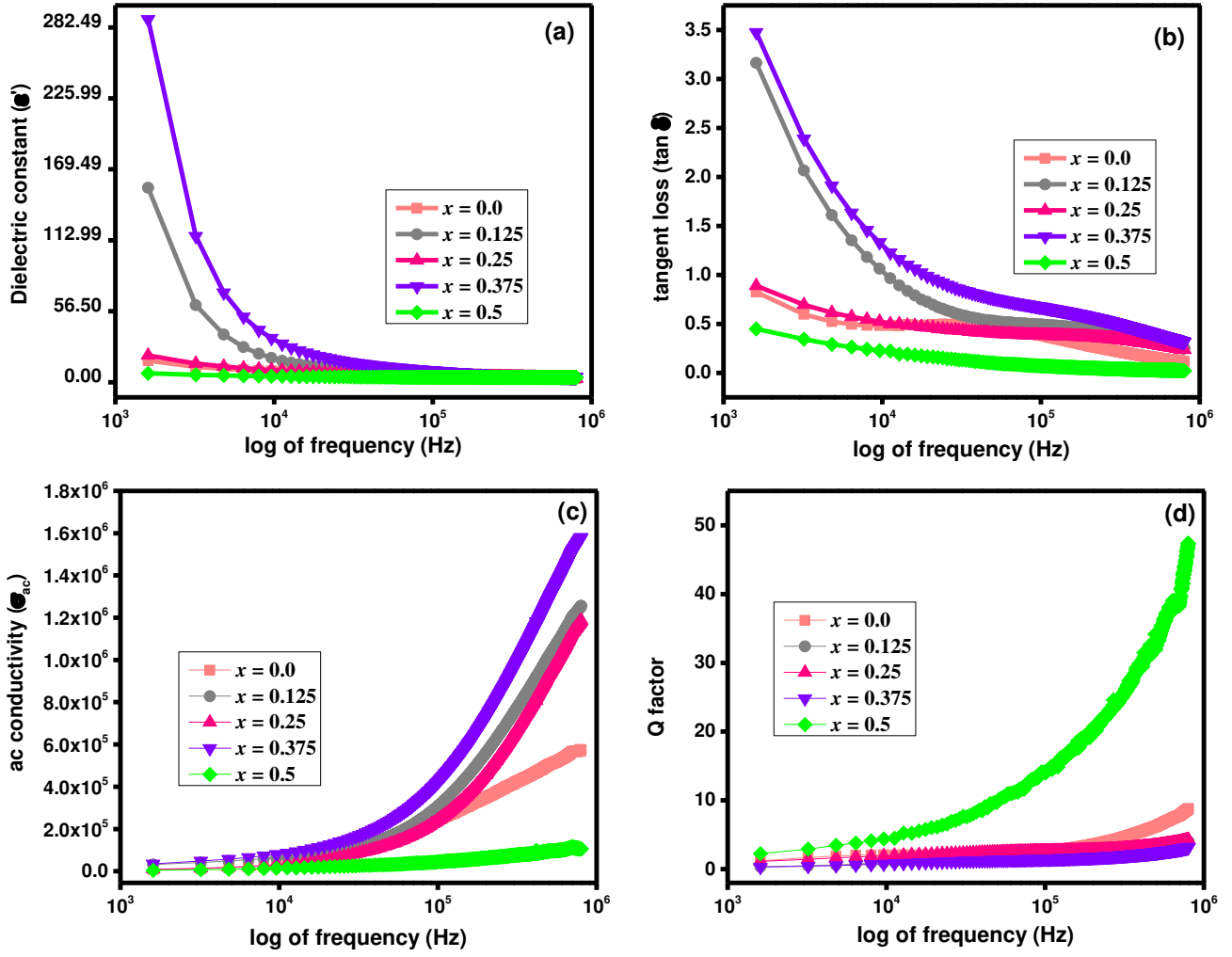


Fig. 10 log of frequency *versus* (a) dielectric constant (b) tangent loss (c) ac conductivity (d)

Quality factor for Co-CCF samples

Fig. 10(c) revealed that at low frequency the ac conductivity is independent of frequency and at high frequency, there is frequency-dependent behavior of conductivity. The ac conductivity (σ_{ac}) of Co-CCF samples is given *via* equation [63];

$$\sigma_{ac} = 2\pi f \tan \delta \quad (15)$$

The Maxwell-Wagner two-layer model described the frequency dependence behavior of conductivity. This model revealed that the grain boundary is further prominent at low frequencies, that's why the hopping frequency of the electrons among cations is small at low frequencies. With a rise in frequency, more active conductive grains facilitate the electron hopping process between Fe²⁺ and Fe³⁺ ions. Consequently, the conductivity rises with a rising in frequency [63]. Quality factor (Q factor) was the evaluation of the relation between deposited

energy and the rate of energy dissipation in definite electrical constituents and gadgets, hence describing their effectiveness. Fig. 10(d) describes the frequency dependence quality factor of Co-CCF samples. Fig. 10(d) revealed that the Quality factor increased with the applied frequency. The higher Q factor ferrites are useful for high-frequency resonant circuits and multilayer chip inductor applications [64]. The tangent loss and Q factor at low (1600 to 12800 Hz) and high (100 to 500 kHz) frequencies are depicted in Fig. 11(a-b) and Fig. 11(c-d), respectively measured at RT. In our current series of Co-CCF samples, the sample with concentration $x = 0.5$ has a greater Q factor and tangent loss was minimum for $x = 0.5$ at low and high frequencies. Therefore, it is better to use for high-frequency resonant circuits and multilayer chip inductors applications.

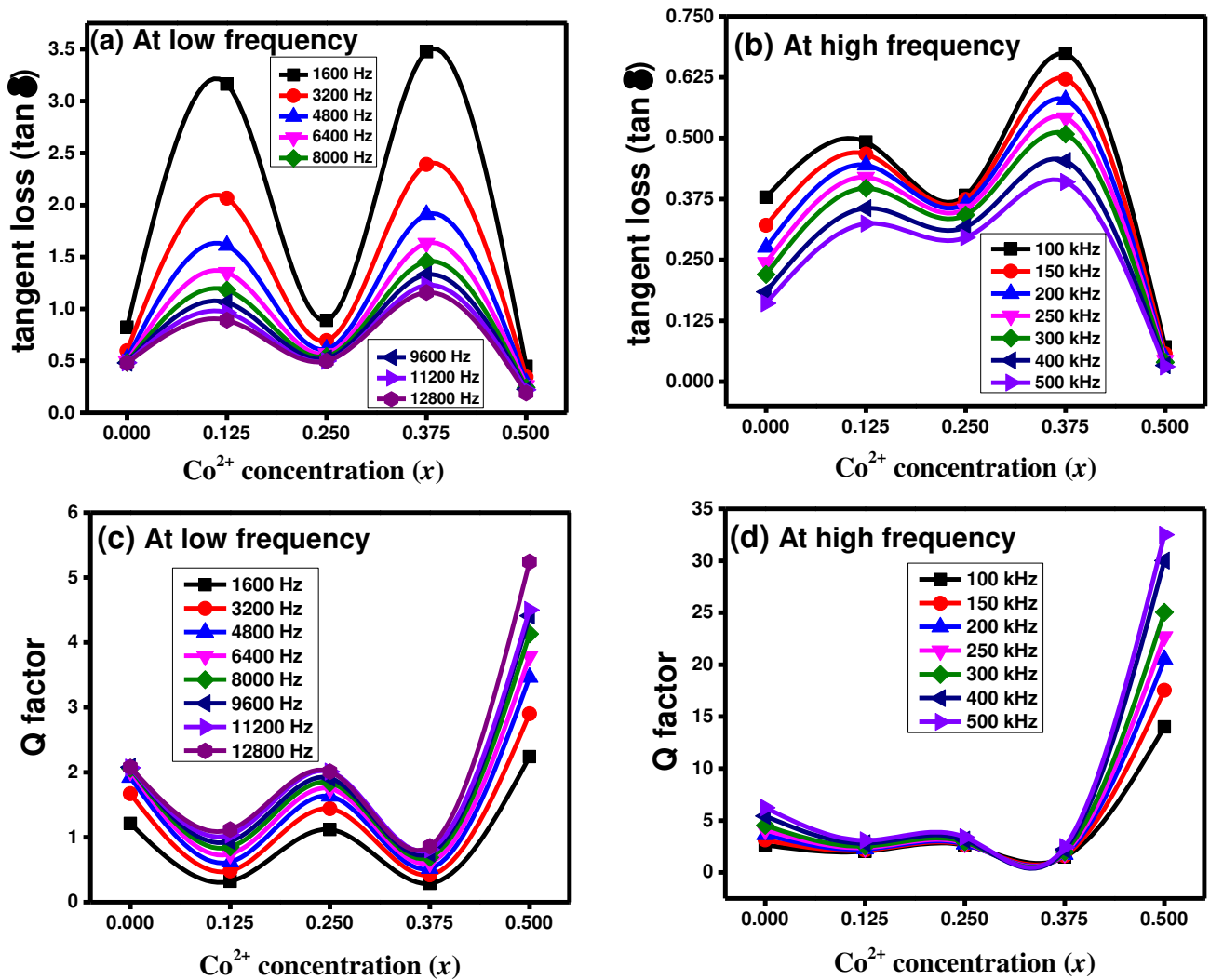


Fig. 11 Co^{2+} concentration (x) versus (a) tangent loss at low frequency (b) tangent loss at high frequency (c) Q factor at low frequency (d) Q factor at high frequency

3.7 Magnetic analysis

The M - H loops for the Co^{2+} doped CCF powder at RT are revealed in Fig. 12(a). The magnetic parameters are listed in Table 6. The replacement of non-magnetic ions in SFs causes a change in M_s , which reaches a maximum with increasing dopant ion concentration and decreases with further increasing concentration of substitute ions. Moreover, the distribution of cations affects also the nonlinear variation of the M_s because the net magnetic moment at a given site is determined by the percentage of the cation present there and their magnetic moment [65]. The saturation magnetization (M_s) was 90.61 emu/g for the pure CCF sample ($x = 0.0$) and for Co^{2+} doping $x = 0.5$ the M_s was 120.85 emu/g. The variation in saturation magnetization of SFs results from the different metal ion magnetic moments at the B - and A - sites in a cubic structure. The nonmagnetic Cd^{2+} ($0 \mu_B$) occupy the A -site [66], and highly magnetic Co^{2+} ($3 \mu_B$) divalent cation and Fe^{3+} ($5 \mu_B$) preferably occupy the A - and B - sites [66]. In SFs, structural parameters including crystallite size, density, and porosity affect the value of M_s for a specific composition [65, 67]. It was clear from Table 1 that the crystallite size was 46.61 nm and saturation magnetization was 128.49 emu/g for $x = 0.375$ sample. The impact of cationic position and their stoichiometry in certain lattice sites is linked to large values of remanent magnetization (M_r) and coercivity (H_c) [68]. The change in H_c depends upon crystallite size, domain structure, anisotropy, and porosity. The increased in H_c is attributed to the increase in the anisotropy [69]. The increased in crystallite size also responsible for the increase in coercivity [70]. The sample's remanent magnetization was minimum for $x = 0.0$ and maximum for $x = 0.0375$. Furthermore, the maximum coercivity was 709.52 Oe for $x = 0.5$. The squareness ratio ($SQ = M_r/M_s$) was enhanced with the substitution of Co^{2+} in the CCF sample. The “ SQ ” ratio, which ranges from 0 to 1, determines whether various sorts of inter-grain group exchanges are absent or exist. According to the literature, $SQ < 0.5$ indicates particle magnetostatic interaction. While $SQ = 0.5$ applies to coherently rotating, randomly oriented, non-interacting particles, and $1 > SQ > 0.5$ indicates the presence of exchange coupling particles [71]. It was observed from Table 6 that the SQ ratio for all the samples has less than 0.5 which indicates the existence of particle magnetostatic interaction. The magnetic anisotropy ($K = \frac{H_c \times M_s}{0.96}$) [52] is significantly affected by rising Co^{2+} in the CCF lattice. With the addition of Co^{2+} , the anisotropy constant was increased, indicating that the magnetic dipoles are more aligned in each direction [72, 73]. The initial permeability ($\mu_i = \frac{M_s^2 \times D}{K}$), where D is crystallite size [52] was maximum for $x = 0.125$ sample.

The applied field *versus* microwave frequency ($\omega_m = 8\pi^2 M_s \gamma$) plots are depicted in Fig. 12(b), where $\gamma = 2.8$ MHz/Oe is a gyromagnetic fraction [34, 74-77]. The “ ω_m ” is directly proportional to the “ M_s ”, as shown by the above relation, and it was clear higher the value of “ M_s ”, the greater will be the value of “ ω_m ”. The values of “ ω_m ” are reported in Table 6 and for $x = 0.0$ (20.03 GHz), while for $x = 0.5$ the value of “ ω_m ” was 26.71 GHz and had a maximum value of 28.40 GHz for $x = 0.375$.

Table 6 Magnetic parameters of as-prepared samples

x	M_s (emu/g)	M_r (emu/g)	H_c (Oe)	SQ	K (erg/cm ³)	μ_i	ω_m (GHz)
0.0	90.61	21.62	74.88	0.238	7067.58	49.21	20.03
0.125	126.73	24.38	69.94	0.192	9232.80	62.20	28.02
0.25	113.65	30.06	156.06	0.264	18475.22	29.55	25.12
0.375	128.49	60.96	536.82	0.474	71850.00	10.71	28.40
0.5	120.85	59.48	709.52	0.492	89318.22	8.31	26.71

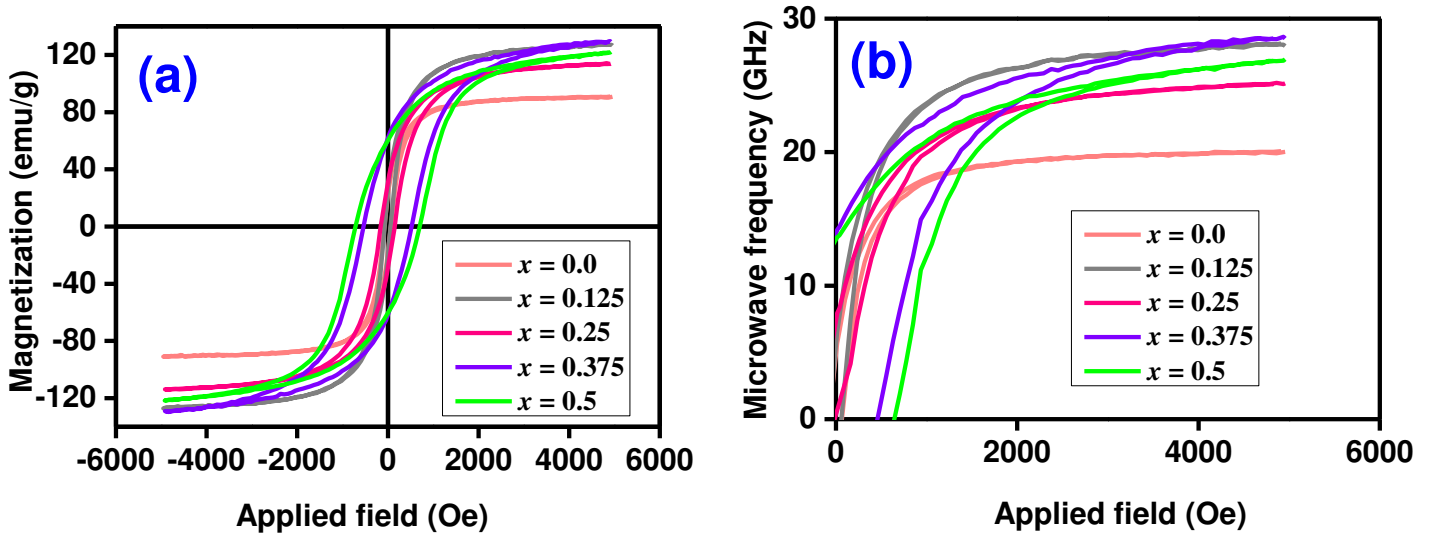


Fig. 12(a) Hysteresis loops for Co^{2+} doped CCF samples **(b)** applied field *versus* microwave frequency

4 Conclusions

Co-CCF SFs were prepared using the SGAC process and the development of a single-phase spinel cubic crystalline matrix was confirmed *via* XRD analysis. The crystal size was 46.61 nm for $x = 0.375$. The A- and B- sites in a spinel matrix are allocated to the higher (ν_1) and lower (ν_2) frequency bands, having ranges (513 – 539 cm^{-1}) and (419 – 472 cm^{-1}), respectively. The change in the structural parameters, absorption, and vibrational bands have confirmed the

replacement of Co^{2+} in the CCF lattice. Moreover, the optical bandgap was 2.44 eV and the resistivity has large values in the order of $10^8 \Omega$ for Co^{2+} doping $x = 0.375$. The dielectric tangent loss and constant showed decreasing behaviour with the rising frequency and both have minimum values with a high Q factor at $x = 0.375$. The microwave frequency and saturation magnetization values for $x = 0.375$ was 28.40 GHz and 128.49 emu/g, respectively with a coercivity was 536.82 Oe. These results suggested that the sample with concentration $x = 0.375$ is a good candidate for high-frequency resonant circuits and multilayer chip inductors applications.

References

- [1] T. Ahmed, I. Rahman, M. Rahman, Study on the properties of the copper substituted NiZn ferrites, *Journal of Materials Processing Technology*, 153 (2004) 797-803.
- [2] D.S. Mathew, R.S. Juang, An overview of the structure and magnetism of spinel ferrite nanoparticles and their synthesis in microemulsions, *Chemical engineering journal*, 129 (2007) 51-65.
- [3] V. Vasanthi, A. Shanmugavani, C. Sanjeeviraja, R.K. Selvan, Microwave assisted combustion synthesis of CdFe_2O_4 : magnetic and electrical properties, *Journal of magnetism and magnetic materials*, 324 (2012) 2100-2107.
- [4] G. Goya, H. Rechenberg, J. Jiang, Structural and magnetic properties of ball milled copper ferrite, *Journal of Applied Physics*, 84 (1998) 1101-1108.
- [5] S. Dalawai, T. Shinde, A. Gadkari, P. Vasambekar, Structural properties of Cd-Co ferrites, *Bulletin of Materials Science*, 36 (2013) 919-922.
- [6] H. Yang, J. Yan, Z. Lu, X. Cheng, Y. Tang, Photocatalytic activity evaluation of tetragonal CuFe_2O_4 nanoparticles for the H_2 evolution under visible light irradiation, *Journal of Alloys and Compounds*, 476 (2009) 715-719.
- [7] L. Jin, Y. Qiu, H. Deng, W. Li, H. Li, S. Yang, Hollow CuFe_2O_4 spheres encapsulated in carbon shells as an anode material for rechargeable lithium-ion batteries, *Electrochimica Acta*, 56 (2011) 9127-9132.
- [8] A. Rocha, L. Magnago, J. Santos, V. Leal, A. Marins, V. Pegoretti, S. Ferreira, M. Lelis, M. Freitas, Copper ferrite synthesis from spent Li-ion batteries for multifunctional application as catalyst in photo Fenton process and as electrochemical pseudocapacitor, *Material Research Bulletin*, 113 (2019) 231-240.
- [9] Y. Fu, Q. Chen, M. He, Y. Wan, X. Sun, H. Xia, X. Wang, Copper ferrite-graphene hybrid: a multifunctional heteroarchitecture for photocatalysis and energy storage, *Industrial and engineering chemistry research*, 51 (2012) 11700-11709.
- [10] Y. Liu, F. Le Formal, F. Boudoire, L. Yao, K. Sivula, N. Guijarro, Insights into the interfacial carrier behaviour of copper ferrite (CuFe_2O_4) photoanodes for solar water oxidation, *Journal of Materials Chemistry A*, 7 (2019) 1669-1677.
- [11] K. Tezuka, M. Kogure, Y.J. Shan, Photocatalytic degradation of acetic acid on spinel ferrites MFe_2O_4 ($\text{M} = \text{Mg}, \text{Zn}, \text{and Cd}$), *Catalysis Communications*, 48 (2014) 11-14.
- [12] Z. Tianshu, P. Hing, Z. Jiancheng, K.J. Lingbing, Ethanol-sensing characteristics of cadmium ferrite prepared by chemical coprecipitation, *Materials Chemistry and physics*, 61 (1999) 192-198.

- [13] V. Nagarajan, A. Thayumanavan, CdFe₂O₄ films for electroresistive detection of ethanol and formaldehyde vapors, *Microchimica Acta*, 185 (2018) 1-9.
- [14] N.-S. Chen, X.J. Yang, E.-S. Liu, J.L. Huang, Reducing gas-sensing properties of ferrite compounds MFe₂O₄ (M = Cu, Zn, Cd and Mg), *Sensors and Actuators B: Chemical*, 66 (2000) 178-180.
- [15] A. Španová, B. Rittich, M.J. Beneš, D. Horák, Ferrite supports for isolation of DNA from complex samples and polymerase chain reaction amplification, *Journal of Chromatography A*, 1080 (2005) 93-98.
- [16] F. Liu, S. Laurent, A. Roch, L. Vander Elst, R.N. Muller, Size-controlled synthesis of CoFe₂O₄ nanoparticles potential contrast agent for MRI and investigation on their size-dependent magnetic properties, *Journal of Nanomaterials*, 2013 (2013) 127.
- [17] S. Amiri, H. Shokrollahi, The role of cobalt ferrite magnetic nanoparticles in medical science, *Materials Science and Engineering: C*, 33 (2013) 1-8.
- [18] F. Choueikani, F. Royer, D. Jamon, A. Siblino, J.J. Rousseau, S. Neveu, J. Charara, Magneto-optical waveguides made of cobalt ferrite nanoparticles embedded in silica/zirconia organic-inorganic matrix, *Applied Physics Letter*, 94 (2009) 051113.
- [19] F.S. Yardımcı, M. Şenel, A. Baykal, Amperometric hydrogen peroxide biosensor based on cobalt ferrite–chitosan nanocomposite, *Materials Science and Engineering: C*, 32 (2012) 269-275.
- [20] T. Yadavalli, H. Jain, G. Chandrasekharan, R. Chennakesavulu, Magnetic hyperthermia heating of cobalt ferrite nanoparticles prepared by low temperature ferrous sulfate based method, *AIP Advances*, 6 (2016) 055904.
- [21] G. Baldi, D. Bonacchi, M.C. Franchini, D. Gentili, G. Lorenzi, A. Ricci, C. Ravagli, Synthesis and coating of cobalt ferrite nanoparticles: a first step toward the obtainment of new magnetic nanocarriers, *Langmuir*, 23 (2007) 4026-4028.
- [22] M. Gabal, M. Ahmed, Structural, electrical and magnetic properties of copper-cadmium ferrites prepared from metal oxalates, *Journal of materials science*, 40 (2005) 387-398.
- [23] W.A. Farooq, M.S. Hasan, M.I. Khan, A.R. Ashraf, M. Abdul Qayyum, N. Yaqub, M.A. Almutairi, M. Atif, A. Hanif, Structural, Optical and Electrical Properties of Cu_{0.6}Co_xZn_{0.4-x}Fe₂O₄ (x = 0.0, 0.1, 0.2, 0.3, 0.4) Soft Ferrites, *Molecules*, 26 (2021) 1399.
- [24] H. Noor ul Huda Khan Asghar, M. Khalid, Z.A. Gilani, M.S. Shifa, A. Parveen, M. Ahmed, J.K. Khan, M. Afzal, F.A. Sheikh, Structural and magnetic properties of Co–Cd–Zn spinel ferrite nanoparticles synthesized through micro-emulsion method, *Optical and Quantum Electronics*, 53 (2021) 1-12.
- [25] K. Hussain, N. Amin, M.I. Arshad, Evaluation of structural, optical, dielectric, electrical, and magnetic properties of Ce³⁺ doped Cu_{0.5}Cd_{0.25}Co_{0.25}Fe_{2-x}O₄ spinel nano-ferrites, *Ceramics International*, 47 (2021) 3401-3410.
- [26] H. Kaur, J. Singh, B. Randhawa, Essence of superparamagnetism in cadmium ferrite induced by various organic fuels via novel solution combustion method, *Ceramics International*, 40 (2014) 12235-12243.
- [27] P. Nordblad, R. Mohan, S. Mukherjee, Structural, magnetic and hyperfine characterizations of nanocrystalline Zn-Cd doped nickel ferrites, *Journal of Magnetism and Magnetic Materials*, 441 (2017) 710-717.
- [28] S. Liang, B. Ravi, S. Sampath, R. Gambino, Atmospheric plasma sprayed cobalt ferrite coatings for magnetostrictive sensor applications, *IEEE Transactions on Magnetics*, 43 (2007) 2391-2393.

- [29] N. Amin, M. Akhtar, M. Sabir, K. Mahmood, A. ALIa, G. Mustafa, M. Hasan, A. Bibi, M. Iqbal, F. Iqbal, SYNTHESIS, STRUCTURAL AND OPTICAL PROPERTIES OF Zn-SUBSTITUTED Co W-FERRITES BY COPRECIPITATION METHOD, *Journal of Ovonic Research*, 16 (2020) 11-19.
- [30] I. ALIa, N. Amin, A. Rehman, M. Akhtar, M. Fatima, K. Mahmood, A. ALIa, G. Mustafa, M. Hasan, A. Bibi, ELECTRICAL AND MAGNETIC PROPERTIES OF $\text{BaCo}_x\text{Cd}_{2-x}\text{Fe}_{16}\text{O}_{27}$ W-TYPE HEXAFERRITES ($0 \leq x \leq 0.5$), *Digest Journal of Nanomaterials and Biostructures*, 15 (2020) 67-73.
- [31] T. Ajeesha, A. Manikandan, A. Anantharaman, S. Jansi, M. Durka, M. Almessiere, Y. Slimani, A. Baykal, A. Asiri, H. Kasmery, Structural investigation of Cu doped calcium ferrite ($\text{Ca}_{1-x}\text{Cu}_x\text{Fe}_2\text{O}_4$; $x = 0, 0.2, 0.4, 0.6, 0.8, 1$) nanomaterials prepared by co-precipitation method, *Journal of Materials Research and Technology*, 18 (2022) 705-719.
- [32] A. Košak, D. Makovec, A. Žnidaršič, M. Drogenik, Preparation of MnZn-ferrite with microemulsion technique, *Journal of the European Ceramic Society*, 24 (2004) 959-962.
- [33] A.U. Rehman, N. Amin, M.B. Tahir, M.A. un Nabi, N. Morley, M. Alzaid, M. Amami, M. Akhtar, M.I. Arshad, Evaluation of spectral, optoelectrical, dielectric, magnetic, and morphological properties of RE^{3+} (La^{3+} , and Ce^{3+}) and Co^{2+} co-doped $\text{Zn}_{0.75}\text{Cu}_{0.25}\text{Fe}_2\text{O}_4$ ferrites, *Materials Chemistry and Physics*, (2021) 125301.
- [34] A.U. Rehman, N. Morley, N. Amin, M.I. Arshad, M.A. un Nabi, K. Mahmood, A. Ali, A. Aslam, A. Bibi, M.Z. Iqbal, Controllable synthesis of La^{3+} doped $\text{Zn}_{0.5}\text{Co}_{0.25}\text{Cu}_{0.25}\text{Fe}_{2-x}\text{La}_x\text{O}_4$ ($x = 0.0, 0.0125, 0.025, 0.0375, 0.05$) nano-ferrites by sol-gel auto-combustion route, *Ceramics International*, 46 (2020) 29297-29308.
- [35] S. Wadgane, S. Alone, A. Karim, G. Vats, S.E. Shirsath, R. Kadam, Magnetic field induced polarization and magnetoelectric effect in $\text{Na}_{0.5}\text{Bi}_{0.5}\text{TiO}_3\text{-Co}_{0.75}\text{Zn}_{0.25}\text{Cr}_{0.2}\text{Fe}_{1.8}\text{O}_4$ multiferroic composite, *Journal of Magnetism and Magnetic Materials*, 471 (2019) 388-393.
- [36] V. More, R. Borade, K. Desai, V. Barote, S. Kadam, V. Shinde, D. Kulkarni, R. Kadam, S. Alone, Site Occupancy, Surface Morphology and Mechanical Properties of Ce^{3+} Added Ni–Mn–Zn Ferrite Nanocrystals Synthesized Via Sol–Gel Route, *Nano*, 16 (2021) 2150059.
- [37] G. Hussain, I. Ahmed, A.U. Rehman, M.U. Subhani, N. Morley, M. Akhtar, M.I. Arshad, H. Anwar, Study of the role of dysprosium substitution in tuning structural, optical, electrical, dielectric, ferroelectric, and magnetic properties of bismuth ferrite multiferroic, *Journal of Alloys and Compounds*, (2022) 165743.
- [38] M. Almessiere, Y. Slimani, H. Güngüneş, A.D. Korkmaz, S. Trukhanov, S. Guner, F. Alahmari, A. Trukhanov, A. Baykal, Correlation between chemical composition, electrical, magnetic and microwave properties in Dy-substituted Ni-Cu-Zn ferrites, *Materials Science and Engineering: B*, 270 (2021) 115202.
- [39] M. Almessiere, Y. Slimani, H. Güngüneş, V. Kostishyn, S. Trukhanov, A. Trukhanov, A. Baykal, Impact of Eu^{3+} ion substitution on structural, magnetic and microwave traits of Ni–Cu–Zn spinel ferrites, *Ceramics International*, 46 (2020) 11124-11131.
- [40] Y. Slimani, M. Almessiere, M. Sertkol, S.E. Shirsath, A. Baykal, M. Nawaz, S. Akhtar, B. Ozcelik, I. Ercan, Structural, magnetic, optical properties and cation distribution of nanosized $\text{Ni}_{0.3}\text{Cu}_{0.3}\text{Zn}_{0.4}\text{Tm}_x\text{Fe}_{2-x}\text{O}_4$ ($0.0 \leq x \leq 0.10$) spinel ferrites synthesized by ultrasound irradiation, *Ultrasonics sonochemistry*, 57 (2019) 203-211.
- [41] X. Jiao, D. Chen, Y. Hu, Hydrothermal synthesis of nanocrystalline $\text{M}_x\text{Zn}_{1-x}\text{Fe}_2\text{O}_4$ ($\text{M} = \text{Ni}, \text{Mn}, \text{Co}$; $x = 0.40\text{--}0.60$) powders, *Material Research Bulletin*, 37 (2002) 1583-1588.

- [42] A. Sutka, G. Mezinskis, Sol-gel auto-combustion synthesis of spinel-type ferrite nanomaterials, *Frontiers of Materials Science*, 6 (2012) 128-141.
- [43] N. Amin, A. Razaq, A.U. Rehman, K. Hussain, M. Nabi, N. Morley, M. Amami, A. Bibi, M.I. Arshad, K. Mahmood, Transport Properties of Ce-Doped Cd Ferrites $\text{CdFe}_{2-x}\text{Ce}_x\text{O}_4$, *Journal of Superconductivity and Novel Magnetism*, (2021) 1-11.
- [44] G. Abbas, A.U. Rehman, W. Gull, M. Afzaal, N. Amin, L. Ben Farhat, M. Amami, N.A. Morley, M. Akhtar, M.I. Arshad, Impact of Co^{2+} on the spectral, optoelectrical, and dielectric properties of $\text{Mg}_{0.25}\text{Ni}_{0.25}\text{Cu}_{0.5-x}\text{Co}_x\text{Fe}_{1.97}\text{La}_{0.03}\text{O}_4$ ferrites prepared via sol-gel auto-combustion route, *Journal of Sol-Gel Science and Technology*, (2022) 1-15.
- [45] E. Hema, A. Manikandan, P. Karthika, S.A. Antony, Venkatraman, A novel synthesis of Zn^{2+} -doped CoFe_2O_4 spinel nanoparticles: structural, morphological, opto-magnetic and catalytic properties, *Journal of Superconductivity and Novel Magnetism*, 28 (2015) 2539-2552.
- [46] G. Sawatzky, F. Van Der Woude, A. Morrish, Cation distributions in octahedral and tetrahedral sites of the ferrimagnetic spinel CoFe_2O_4 , *Journal of Applied Physics*, 39 (1968) 1204-1205.
- [47] D. Thapa, N. Kulkarni, S. Mishra, P. Paulose, P. Ayyub, Enhanced magnetization in cubic ferrimagnetic CuFe_2O_4 nanoparticles synthesized from a citrate precursor: the role of Fe^{2+} , *Journal of Physics D: Applied Physics*, 43 (2010) 195004.
- [48] R. Zakir, S.S. Iqbal, A.U. Rehman, S. Nosheen, T.S. Ahmad, N. Ehsan, F. Inam, Spectral, electrical, and dielectric characterization of Ce-doped Co-Mg-Cd spinel nano-ferrites synthesized by the sol-gel auto combustion method, *Ceramics International*, 47 (2021) 28575-28583.
- [49] A. Aslam, A.U. Rehman, N. Amin, M. Amman, M. Akhtar, N. Morley, M.S. Al-Sharif, M. Hessian, K.A. El-Nagdy, M.I. Arshad, To study the structural, electrical, and magnetic properties of M ($\text{M} = \text{Mg}^{2+}$, Mn^{2+} , and Cd^{2+}) doped Cu-Ni-Co-La spinel ferrites, *Materials Chemistry and Physics*, (2022) 127034.
- [50] A. Aslam, A.U. Rehman, N. Amin, M. Amami, M. Nabi, H. Alrobei, M. Asghar, N. Morley, M. Akhtar, M.I. Arshad, Sol-Gel Auto-combustion Preparation of $\text{M}^{2+} = \text{Mg}^{2+}$, Mn^{2+} , Cd^{2+} Substituted $\text{M}_{0.25}\text{Ni}_{0.15}\text{Cu}_{0.25}\text{Co}_{0.35}\text{Fe}_2\text{O}_4$ Ferrites and Their Characterizations, *Journal of Superconductivity and Novel Magnetism*, (2021) 1-11.
- [51] K. Jalaiah, K.C. Mouli, R. Krishnaiah, K.V. Babu, P.S. Rao, The structural, DC resistivity and magnetic properties of Zr and Co co-substituted $\text{Ni}_{0.5}\text{Zn}_{0.5}\text{Fe}_2\text{O}_4$, *Heliyon*, 5 (2019) e01800.
- [52] K. Hussain, A. Bibi, F. Jabeen, N. Amin, K. Mahmood, A. Ali, M.Z. Iqbal, M. Arshad, Study of structural, optical, electrical and magnetic properties of Cu^{2+} doped $\text{Zn}_{0.4}\text{Co}_{0.6-x}\text{Ce}_{0.1}\text{Fe}_{1.9}\text{O}_4$ spinel ferrites, *Physica B: Condensed Matter*, 584 (2020) 412078.
- [53] M. Lakshmi, K. Vijaya Kumar, K. Thyagarajan, An investigation of structural and magnetic properties of Cr-Zn ferrite nanoparticles prepared by a sol-gel process, *Journal of Nanostructure in Chemistry*, 5 (2015) 365-373.
- [54] A. Aslam, A.U. Rehman, N. Amin, M.A. un Nabi, Q. ul ain Abdullah, N. Morley, M.I. Arshad, H.T. Ali, M. Yusuf, Z. Latif, Lanthanum doped $\text{Zn}_{0.5}\text{Co}_{0.5}\text{La}_x\text{Fe}_{2-x}\text{O}_4$ spinel ferrites synthesized via co-precipitation route to evaluate structural, vibrational, electrical, optical, dielectric, and thermoelectric properties, *Journal of Physics and Chemistry of Solids*, 154 (2021) 110080.
- [55] A. Aslam, N. Morley, N. Amin, M.I. Arshad, M.A. un Nabi, A. Ali, K. Mahmood, A. Bibi, F. Iqbal, S. Hussain, Study of structural, optical and electrical properties of La^{3+} doped $\text{Mg}_{0.25}\text{Ni}_{0.15}\text{Cu}_{0.25}\text{Co}_{0.35}\text{Fe}_{2-x}\text{La}_x\text{O}_4$ spinel ferrites, *Physica B: Condensed Matter*, 602 (2021) 412565.

- [56] L. Phor, S. Chahal, V. Kumar, Zn²⁺ substituted superparamagnetic MgFe₂O₄ spinel-ferrites: Investigations on structural and spin-interactions, *Journal of Advanced Ceramics*, 9 (2020) 576-587.
- [57] A. Kumar, P. Sharma, D. Varshney, Structural, vibrational and dielectric study of Ni doped spinel Co ferrites: Co_{1-x}Ni_xFe₂O₄ (x = 0.0, 0.5, 1.0), *Ceramics International*, 40 (2014) 12855-12860.
- [58] A. Aslam, A. Razzaq, S. Naz, N. Amin, M.I. Arshad, M. Nabi, A. Nawaz, K. Mahmood, A. Bibi, F. Iqbal, Impact of lanthanum-doping on the physical and electrical properties of cobalt ferrites, *Journal of Superconductivity and Novel Magnetism*, 34 (2021) 1855-1864.
- [59] A. Patil, S. Patange, P.M. Dighe, S.F. Shaikh, B. Pandit, S.S. Jadhav, Tuning the structural, optical and magnetic properties of NiCuZn (Ni_{0.4}Cu_{0.3}Zn_{0.3}Fe₂O₄) spinel ferrites by Nb₂O₅ additive, *Ceramics International*, 48 (2022) 27039-27050.
- [60] A.D. Patil, R.A. Pawar, S.M. Patange, S.S. Jadhav, S.K. Gore, S.E. Shirsath, S.S. Meena, TiO₂-doped Ni_{0.4}Cu_{0.3}Zn_{0.3}Fe₂O₄ nanoparticles for enhanced structural and magnetic properties, *ACS omega*, 6 (2021) 17931-17940.
- [61] S. Yousaf, I. Ahmad, M. Kanwal, T. Alshahrani, H.H. Alhashim, N.A. Kattan, H.M.T. Farid, A. Riaz, T. Mehran, A. Laref, Structural and electrical properties of Ba-substituted spinel ferrites, *Materials Science in Semiconductor Processing*, 122 (2021) 105488.
- [62] S. Aman, M.B. Tahir, N. Ahmad, The enhanced electrical and dielectric properties of cobalt-based spinel ferrites for high-frequency applications, *Journal of Materials Science: Materials in Electronics*, 32 (2021) 22440-22449.
- [63] R.S. Yadav, I. Kuřitka, J. Vilcakova, J. Havlica, J. Masilko, L. Kalina, J. Tkacz, J. Švec, V. Enev, M. Hajdúchová, Impact of grain size and structural changes on magnetic, dielectric, electrical, impedance and modulus spectroscopic characteristics of CoFe₂O₄ nanoparticles synthesized by honey mediated sol-gel combustion method, *Advances in Natural Sciences: Nanoscience and Nanotechnology*, 8 (2017) 045002.
- [64] M. Junaid, J. Jacob, M. Nadeem, N. Jabbar, M.A. Khan, A. Manzoor, A.H. Chughtai, A. Ali, K. Mahmood, S. Hussain, Structural elucidation and dielectric behavior evaluation of Dy–Ni substituted manganese ferrites, *Physica B: Condensed Matter*, 602 (2021) 412494.
- [65] J. Shitole, S. Keshatti, S. Rathod, S.S. Jadhav, Y³⁺ composition and particle size influenced magnetic and dielectric properties of nanocrystalline Ni_{0.5}Cu_{0.5}Y_xFe_{2-x}O₄ ferrites, *Ceramics International*, 47 (2021) 17993-18002.
- [66] H. Ghorbani, M. Eshraghi, A.S. Dodaran, Structural and magnetic properties of cobalt ferrite nanoparticles doped with cadmium, *Physica B: Condensed Matter*, 634 (2022) 413816.
- [67] S.M. Rathod, A.R. Chavan, S.S. Jadhav, K.M. Batoo, M. Hadi, E.H. Raslan, Ag ion substituted CuFe₂O₄ nanoparticles: Analysis of structural and magnetic behavior, *Chemical Physics Letters*, 765 (2021) 138308.
- [68] J. Feng, R. Xiong, Y. Liu, F. Su, X. Zhang, Preparation of cobalt substituted zinc ferrite nanopowders via auto-combustion route: An investigation to their structural and magnetic properties, *Journal of Materials Science: Materials in Electronics*, 29 (2018) 18358-18371.
- [69] A.B. Mugutkar, S.K. Gore, U.B. Tumberphale, V.V. Jadhav, R.S. Mane, S.M. Patange, S.F. Shaikh, M. Ubaidullah, A.M. Al-Enizi, S.S. Jadhav, The role of La³⁺ substitution in modification of the magnetic and dielectric properties of the nanocrystalline Co-Zn ferrites, *Journal of Magnetism and Magnetic Materials*, 502 (2020) 166490.
- [70] A.B. Mugutkar, S.K. Gore, U.B. Tumberphale, V.V. Jadhav, R.S. Mane, S.M. Patange, S.E. Shirsath, S.S. Jadhav, Role of composition and grain size in controlling the structure sensitive

magnetic properties of Sm^{3+} substituted nanocrystalline Co-Zn ferrites, *Journal of Rare Earths*, 38 (2020) 1069-1075.

[71] E.E. Ateia, A.A. El-Bassuony, G. Abdelatif, F. Soliman, Novelty characterization and enhancement of magnetic properties of Co and Cu nanoferrites, *Journal of Materials Science: Materials in Electronics*, 28 (2017) 241-249.

[72] M.N. Akhtar, M.A. Khan, Effect of rare earth doping on the structural and magnetic features of nanocrystalline spinel ferrites prepared via sol gel route, *Journal of Magnetism and Magnetic Materials*, 460 (2018) 268-277.

[73] T.R. Tatarchuk, N.D. Paliychuk, M. Bououdina, B. Al-Najar, M. Pacia, W. Macyk, A. Shyichuk, Effect of cobalt substitution on structural, elastic, magnetic and optical properties of zinc ferrite nanoparticles, *Journal of Alloys and Compounds*, 731 (2018) 1256-1266.

[74] A. Majeed, M.A. Khan, F. ur Raheem, A. Hussain, F. Iqbal, G. Murtaza, M.N. Akhtar, I. Shakir, M.F. Warsi, Structural elucidation and magnetic behavior evaluation of rare earth (La, Nd, Gd, Tb, Dy) doped BaCoNi-X hexagonal nano-sized ferrites, *Journal of magnetism and magnetic materials*, 408 (2016) 147-151.

[75] S. Gaba, A. Kumar, P.S. Rana, M. Arora, Influence of La^{3+} ion doping on physical properties of magnesium nanoferrites for microwave absorption application, *Journal of Magnetism and Magnetic Materials*, 460 (2018) 69-77.

[76] A.U. Rehman, N. Amin, M.B. Tahir, M.A. un Nabi, N. Morley, M. Alzaid, M. Amami, M. Akhtar, M.I. Arshad, Evaluation of spectral, optoelectrical, dielectric, magnetic, and morphological properties of RE^{3+} (La^{3+} , and Ce^{3+}) and Co^{2+} co-doped $\text{Zn}_{0.75}\text{Cu}_{0.25}\text{Fe}_2\text{O}_4$ ferrites, *Materials Chemistry and Physics*, 275 (2022) 125301.

[77] M.I. Arshad, M. Hasan, A.U. Rehman, M. Akhtar, N. Amin, K. Mahmood, A. Ali, T. Trakoolwilaiwan, N.T.K. Thanh, Structural, optical, electrical, dielectric, molecular vibrational and magnetic properties of La^{3+} doped Mg–Cd–Cu ferrites prepared by Co-precipitation technique, *Ceramics International*, 48 (2022) 14246-14260.